Solid Freeform Fabrication 2024: Proceedings of the 35th Annual International Solid Freeform Fabrication Symposium – An Additive Manufacturing Conference
Reviewed Paper

Effect of Heat Treatment on the Micro-/Defect-structure and Mechanical Behavior of Additively Manufactured AlF357 Aluminum Alloy

Md Faysal Khan[1,2], Paul R. Gradl[3], Donald Godfrey[4], Jacky Diemann[5], Shuai Shao[1,2], Nima Shamsaei[1,2*]

[1]National Center for Additive Manufacturing Excellence (NCAME), Auburn University, Auburn, AL 36849, USA

[2]Department of Mechanical Engineering, Auburn University, Auburn, AL 36849, USA

[3]Propulsion Department, NASA Marshall Space Flight Center, Huntsville, Al 35812, USA

[4]Nikon SLM Solutions NA, Inc. Long Beach, CA 90808, USA

[5]Nikon SLM Solutions Group AG, Lübeck, Germany

* Corresponding author:

Email: shamsaei@auburn.edu

Tel: (334) 844 4839

Abstract

This study investigated the effect of heat treatment (HT) on the micro-/defect-structure and room temperature tensile and fatigue behaviors of AlF357 fabricated using laser powder bed fusion. Two different HT sequences, consisting of stress relieving (SR), hot isostatic pressing (HIP), and T6 (i.e., SR+HIP+T6 and SR+T6+HIP), were examined. For SR+T6+HIP, all defects still present after T6 were eliminated after the final HIP. For SR+HIP+T6, a few defects closed following HIP had reopened. The grain structure remained comparable for both HTs. SR+HIP+T6 resulted in approximately 45% and 32% higher yield and ultimate tensile strength, respectively, due to increased Mg_2Si precipitate population and size compared to SR+T6+HIP. However, the presence of large and populous π-Fe ($Al_8Mg_3FeSi_6$) precipitates lowered ductility by around 6% for SR+HIP+T6 compared to SR+T6+HIP. Specimens in SR+HIP+T6 showed higher fatigue resistance for the alloy than those in SR+T6+HIP.

Keywords: Laser powder bed fusion (L-PBF), AlF357, Heat treatment, Micro-/defect- structure, Tensile and fatigue behavior

Introduction

AlF357 is a cast aluminum alloy in the Al-7Si-Mg family widely employed in defense, aerospace, and automotive industries due to its lightweight, good corrosion resistance, and good strength-to-weight ratio [1][2]. It is a Beryllium-free variant of the A357 alloy, avoiding the toxicity issue of that element [3]. AlF357 alloy emerges as an excellent option for additive manufacturing (AM) due to its good weldability, and suitability for the complex geometry of components required in aerospace and automotive industries [4]. Laser powder bed fusion (L-PBF) is a specific AM technology utilizing powder-bed technology, particularly suited for fabricating complex-shaped structural and functional components [5]. Due to its high cooling rates, the L-PBF process induces unique microstructural features in the alloy. A suitable post-process heat treatment (HT) can optimize the microstructure and phase composition, thereby enhancing the alloy's mechanical properties [6][7].

The effect of HT, involving stress relief (SR), solutionizing, aging, and specifically T6 (e.g., solutionizing, quenching, and artificial aging) conditions on microstructure and mechanical properties of L-PBF AlF357 alloy has been studied in the literature. SR aims to reduce residual stresses from the fabrication process without altering the as-built microstructure. Solution treatment helps the precipitation of fine Si particles from the supersaturated Al Matrix, which coarsen with increasing solution temperature. Aging enhances the tensile strength by precipitating the fine Mg_2Si strengthening phase. However, various studies indicate that T6 treatment has the potential to exacerbate the existing defects in Al-Si-Mg alloys [8][9][10], which will directly influence their fatigue resistance. Therefore, the investigation of different post-processing treatments (e.g., hot isostatic pressing) is necessary to better understand the correlation between micro-/defect-structure and the mechanical properties of the alloy. However, the tensile strength of other L-PBF Al-Si alloys, i.e., AlSi10Mg [11], AlSi12 [12], and AlSi20 [13], have been reported to decrease following HIP treatment, although with a ductility increase.

This study investigated the influence of two different HT conditions, i.e., SR+HIP+T6 and SR+T6+HIP, on the micro-/defect-structure and room temperature tensile and fatigue behaviors of additively manufactured (AM) AlF357 aluminum alloy fabricated via L-PBF.

Experimental Procedure

The specimens in this study were fabricated using pre-alloyed, gas atomized AlF357 powders provided by IMR Metal Powder Technologies GmbH with a powder particle size range of 20-63 μm. The particle size distribution was measured via laser diffraction particle size analysis, yielding D_{10} = 26.4 μm, D_{50} = 39.7 μm, and D_{90} = 59.7 μm. The chemical composition of the powder, measured by the powder supplier using inductively coupled plasma-optical emission spectrometry (ICP-OES), is listed in **Table 1**. Cylindrical rods with 15 mm diameter and 316 mm length were fabricated vertically via L-PBF using an SLM280 2.0 machine using the following process parameters: laser power of 370 W, scanning speed of 1225 mm/s, hatch spacing of 0.1 mm, and layer thickness of 30 μm. Ar was used as a shielding gas during fabrication.

Table 1. Chemical composition of AlF357 powder used in this study, obtained via ICP-OES by IMR Metal Powder Technologies GmbH.

Element	**Al**	**Si**	**Mg**	**Fe**	**Cu**	**Mn**	**Ti**	**Zn**	**Pb**
(wt.%)	Bal.	7.10	0.56	0.078	0.001	0.001	0.07	0.002	0.001
Element	**Ni**	**V**	**Zr**	**O**	**H**	**N**			
(wt.%)	0.003	0.008	0.001	0.019	0.002	<0.002			

After fabrication, the cylindrical bars went through multiple steps of HTs, including stress relieving (SR at 300 °C for 2 hrs followed by furnace cooling), hot isostatic pressing (HIP at 520 °C under 100 MPa isostatic pressure for 2 hrs followed by furnace cooling), and T6 (solutionizing at 520 °C for 2 hrs followed by water quenching, and aging at 165 °C for 4 hrs followed by air cooling). Two batches of cylindrical rods were heat-treated (HT), i.e., SR+HIP+T6 and SR+T6+HIP, to evaluate the resulting microstructure, defect content, and room temperature tensile and fatigue properties. The schematic diagrams of two HT schedules are presented in **Figure 1**. Following HTs, the cylindrical rods were machined to the final geometry of the tensile and fatigue test specimens according to ASTM E8 and ASTM E606 standards, respectively (see **Figure 2**).

Microstructural characterization of L-PBF AlF357 was performed on samples taken from both the longitudinal plane (LP), which was parallel with the build direction, and the radial plane (RP), perpendicular to the build direction. Small sections from the middle of the specimens were used for the characterization. These samples were embedded in epoxy resin and polished to a mirror finish according to ASTM E3 [14]. The analysis was carried out using a Zeiss 550 scanning electron microscope (SEM) equipped with electron backscatter diffraction (EBSD) and energy-dispersive spectroscopy (EDS) detectors. The inverse pole figure map was employed to determine grain size, while backscattered electron (BSE) imaging was utilized for generating detailed micrographs using the electron contrast channeling technique.

The X-ray computed tomography (X-CT) was conducted on a 5 mm diameter and 5 mm height coupon, machined from the mid-section of the cylindrical bars, to evaluate the volumetric defect contents in different HT conditions. Scans were performed using a Zeiss Xradia 620 Versa system with a 60 kV accelerating voltage, 6.5 W power, and 5.3 μm voxel size. Volumetric reconstruction was done using Zeiss proprietary software, followed by image analysis using ImageJ and Dragonfly software.

Room temperature tensile tests were performed at a strain rate of 0.005 mm/mm/min according to the ASTM E8 standard [15]. During testing, strains were measured using an extensometer attached to the gage section of specimens to measure the yield strength of the specimens until 0.035 mm/mm strain. After that, the extensometer was removed due to its limited travel, and then the test was continued in displacement control until complete fracture. At least three specimens were tested at room temperature for both batches and their average values were reported.

Strain-controlled, uniaxial, fully reversed ($R_\varepsilon = \varepsilon_{min}/\varepsilon_{max} = -1$) fatigue tests were performed utilizing an MTS servo-hydraulic machine according to the ASTM E606 standard [16]. Two

different strain amplitudes, 0.003 mm/mm and 0.002 mm/mm were applied at frequencies of 0.83 Hz and 1.25 Hz, respectively. At least three specimens were tested for each strain amplitude using a triangular waveform with a strain rate of 0.010 mm/mm/sec. Fatigue tests were continued until specimen fracture or predefined runout condition (10^7 reversals) was reached. Fractography was performed using SEM on selected tensile and fatigue fracture surfaces to study the tensile fracture mechanisms and identify the locations of fatigue crack initiation. After tensile and fatigue failures, the fracture surfaces were examined using SEM to understand the tensile fracture mechanisms and identify the locations of fatigue crack initiation.

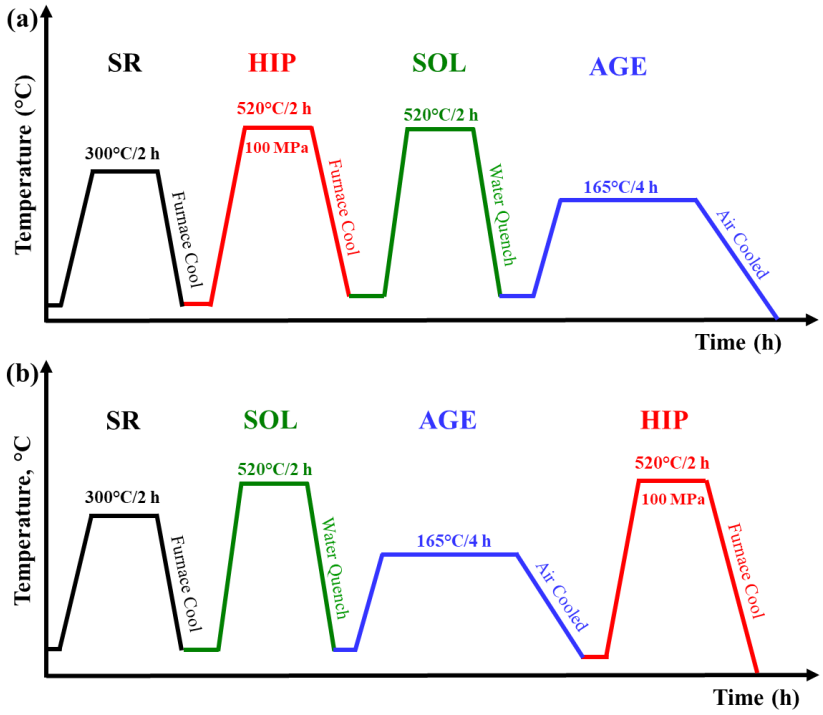

Figure 1. Schematic diagrams of two HTs conducted in this study on L-PBF AlF357 cylindrical rods: (a) SR+HIP+T6, and (b) SR+T6+HIP.

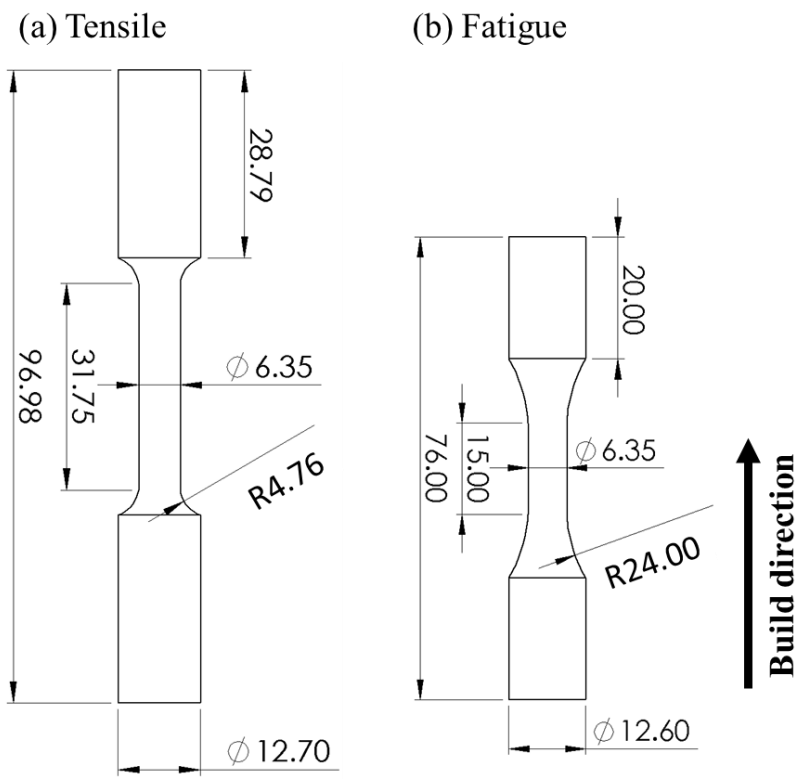

Figure 2. Geometries of L-PBF AlF357 (a) tensile and (b) fatigue test specimens following ASTM E8 and ASTM E606, respectively. Note that all the dimensions are in 'mm'.

Results and Discussion

The inverse pole figure (IPF) maps obtained from the LP and RP of L-PBF AlF357 coupons in non-heat treated (NHT) and two fully HT (i.e., SR+HIP+T6 and SR +T6+HIP) conditions are shown in **Figure 3**. At the top of each IPF map in **Figure 3**, the average grain size in equivalent circle diameter, alongside standard deviations, is displayed. These grain size measurements were obtained using EBSD analysis. The grains exhibited a columnar shape on LP and were equiaxed on RP. In the NHT condition, the average grain sizes on the LP and RP were 7.8±5.6 μm and 6.5±3.2 μm, respectively (see **Figure 3** (a)-(b)). In both HT conditions, the grain structure slightly coarsened on both planes. However, the grain structures remained comparable between the two HT conditions. The average grain sizes were 11.4±8.6 μm and 9.4±5.1 μm on the LP and RP, respectively, in the SR+HIP+T6 condition, and 11.5±8.4 μm and 9.1±4.2 μm on the LP and RP, respectively, in the SR+T6+HIP condition.

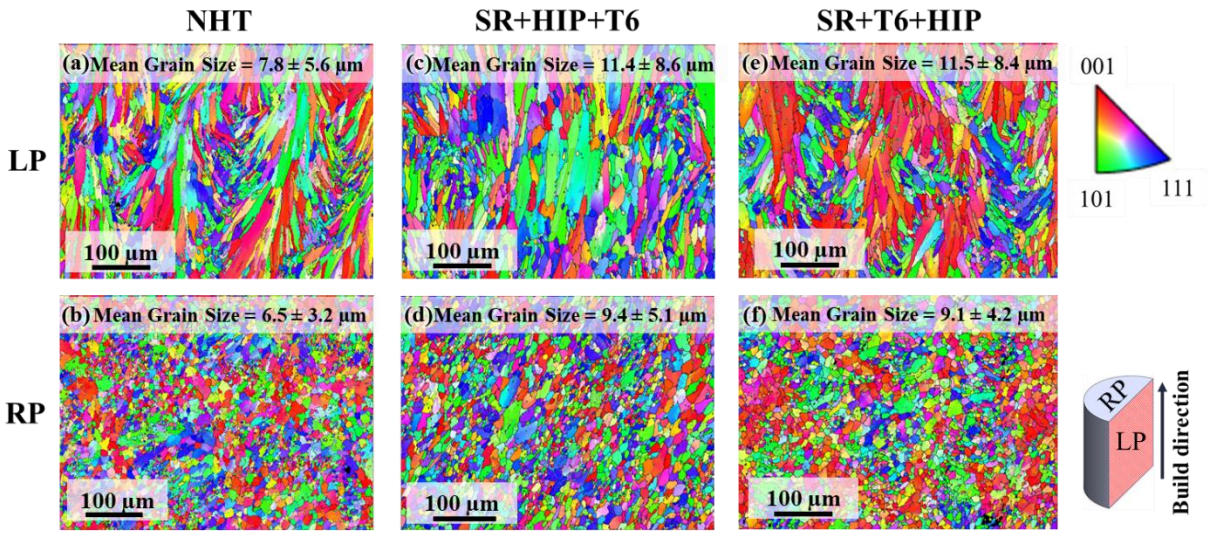

Figure 3. IPF maps obtained from EBSD analysis from both longitudinal (LP) and radial (RP) planes for L-PBF AlF357 specimens in (a)-(b) NHT, (c)-(d) SR+HIP+T6, and (e)-(f) SR+T6+HIP conditions.

The BSE micrographs of L-PBF AlF357 coupons of the LP in three different conditions — NHT, SR+HIP+T6, and SR+T6+HIP—are presented in **Figure 4,** shown at two magnifications. In NHT condition, micrographs revealed α-Al surrounded by a cellular Si network, a result of the rapid cooling and solidification inherent to the L-PBF process [17][18]. Upon full HT for both conditions, the dendritic microstructure dissolved, leaving Si particles distributed in the α-Al matrix. Additionally, small Mg_2Si and π-Fe ($Al_8Mg_3FeSi_6$) phases precipitated after the full HT. The EDS elemental maps, presented in **Figure 5**, confirm the presence of these precipitates in both HT conditions. However, the shape and size of these precipitates varied depending on the sequence of HT steps. The size of the Mg_2Si and π-Fe precipitates was larger in the SR+HIP+T6 treated microstructure due to the final artificial aging step (see **Figure 4** (c)-(d) and **Figure 5** (a)). However, for the SR+T6+HIP condition, the HIP after the artificial aging must have dissolved some of these precipitates, leading to a smaller size and population compared to SR+HIP+T6 (see **Figure 4** (e)-(f) and **Figure 5** (b)). These variations in precipitate population and size between the two HT conditions may impact the tensile properties of the alloy.

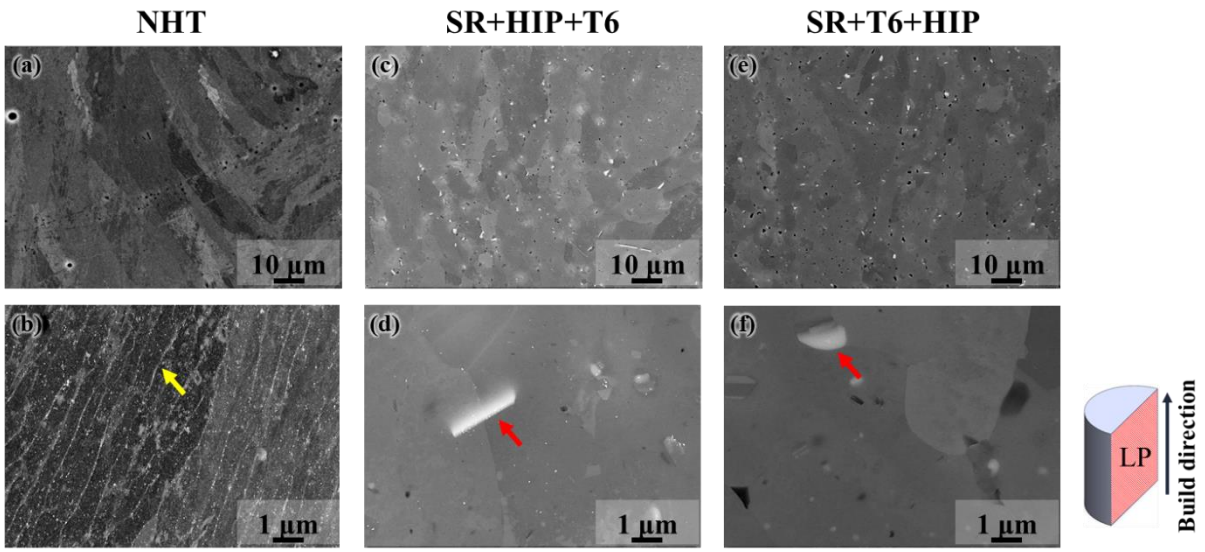

Figure 4. The BSE images for L-PBF AlF357 alloy in different HT conditions: (a)-(b) NHT, (c)-(d) SR+HIP+T6, and (e)-(f) SR+T6+HIP. The yellow and red arrows indicate dendritic Si network and π-Fe precipitate, respectively.

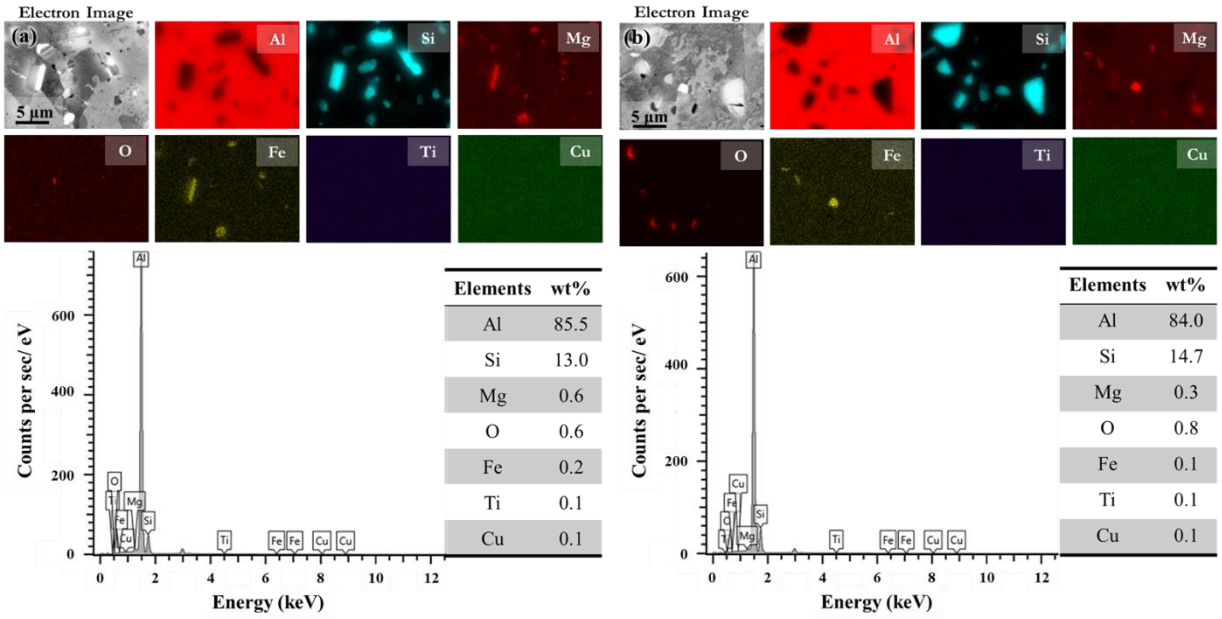

Figure 5. Results from EDS analysis, the elemental maps for L-PBF AlF357 in fully HT conditions: (a) SR+HIP+T6 and (b) SR+T6+HIP.

The X-CT results, including porosity contents of the L-PBF AlF357 coupons in NHT, SR+T6, SR+HIP+T6, and SR+T6+HIP conditions, are presented in **Figure 6** (a)-(d). The porosity contents for all HT conditions are quantitatively presented as a histogram in **Figure 6** (e). The same coupon was scanned in NHT, SR+T6, and SR+T6+HIP conditions. The defect population in the SR+T6 condition was slightly higher than that in the NHT condition, which indicated that T6 opened pores from the NHT condition (see **Figure 6** (a)-(b)). However, the scan result of the coupon underwent SR+T6 followed by HIP showed no defect. SR+HIP followed by T6, a few defects reappeared in the coupon at a relative density of 99.99% and the maximum defect size measured 37 µm.

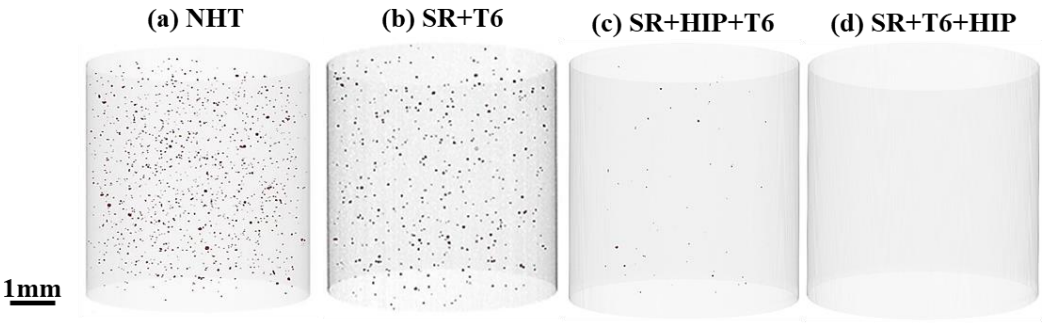

Relative density	99.60%	99.43%	99.99%	100%
Max. pore dia.	80 µm	81 µm	37 µm	-

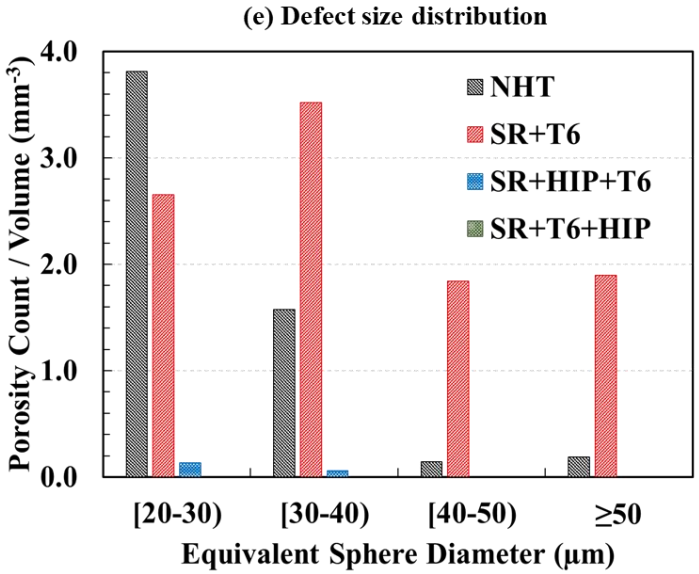

Figure 6. X-CT scan results for L-PBF AlF357 coupons in NHT, SR+T6, SR+HIP+T6, and SR+T6+HIP conditions using (a)-(d) 3D visualization of volumetric defects and (e) the corresponding defect size distributions.

The room temperature engineering stress-strain curves of L-PBF AlF357 specimens under SR+HIP+T6 and SR+T6+HIP conditions are plotted in **Figure 7** (a). Additionally, **Figure 7** (b) presents the bar chart for the quasi-static tensile properties of L-PBF AlF357, including yield strength (YS), ultimate tensile strength (UTS), and elongation to failure (EL), under different HT conditions. For comparison, the chart also includes the tensile properties of L-PBF AlF357 in NHT condition from the literature. The SR+HIP+T6 treated specimens showed 45% and 32% higher YS and UTS, respectively, compared to the SR+T6+HIP ones. However, specimens exhibited a 6% lower EL in the SR+HIP+T6 condition compared to SR+T6+HIP.

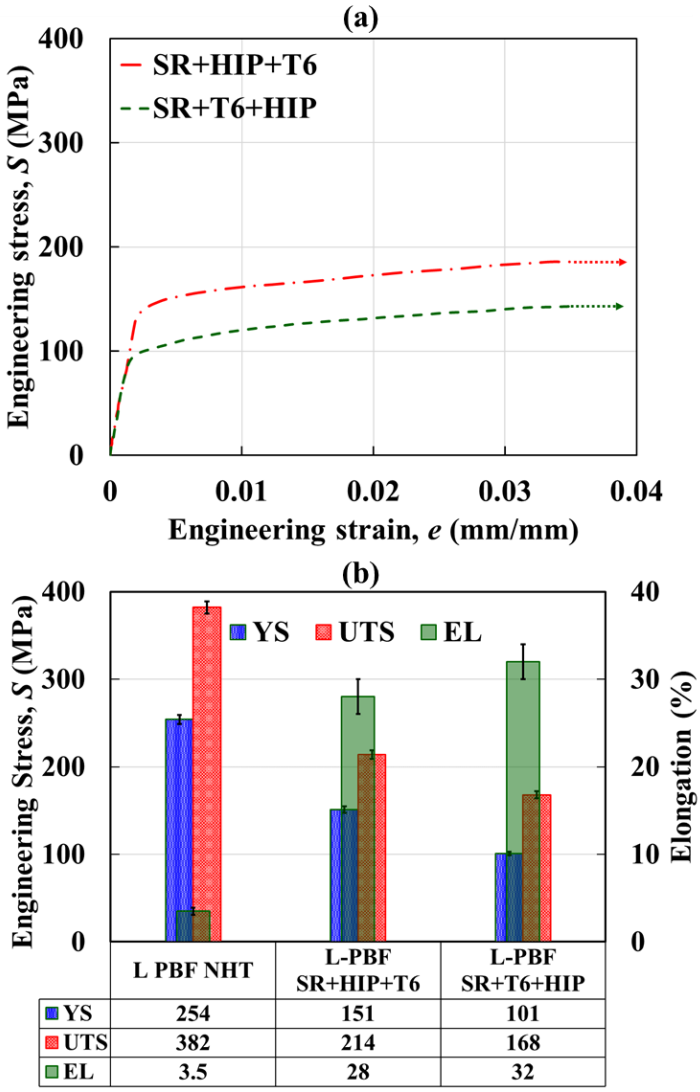

Figure 7. Room temperature tensile behavior of L-PBF AlF357 in different HT conditions: (a) engineering stress-strain curves, and (b) comparative bar charts for tensile properties of L-PBF AlF357 in SR+HIP+T6 and SR +T6+HIP conditions along with in NHT condition from the literature. The arrows on the stress-strain curves indicate that the extensometer was removed at approximately 0.35 mm/mm strain, and the tests resumed under displacement control.

The higher tensile strength of AlF357 in the SR+HIP+T6 condition can be ascribed to the increased population and size of the Mg_2Si precipitates compared to the SR+T6+HIP condition. The lower EL in the SR+HIP+T6 condition can be attributed to the presence of large and populous π-Fe ($Al_8Mg_3FeSi_6$) precipitates. The fractography of tensile fracture surfaces for the two HT conditions is presented in **Figure 8** (a)-(b) and **Figure 8** (g)-(h). The presence of Si, Mg_2Si, and π-Fe particles on the fracture surfaces has been confirmed by EDS elemental maps (see **Figure 8** (c)-(f) and **Figure 8** (i)-(l)). These Si particles within the dimples are responsible for fracture by void nucleation. Furthermore, the larger size of Si particles in the SR+HIP+T6 treated specimens can act as higher stress concentrators, reducing the overall ductility of the alloy compared to the SR+T6+HIP treated specimens.

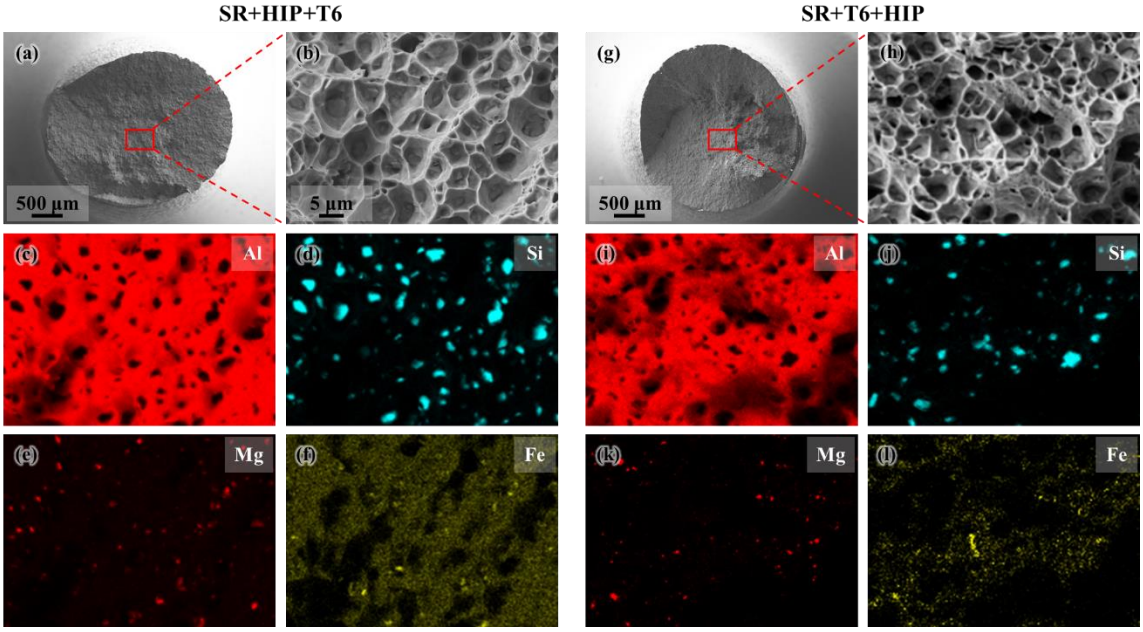

Figure 8. Tensile fracture surfaces along with the EDS elemental maps of L-PBF AlF357 specimens in two HT conditions: (a)-(f) SR+HIP+T6 and (g)-(l) SR+T6+HIP.

The strain-life fatigue plot of L-PBF AlF357 specimens in SR+HIP+T6 and SR+T6+HIP conditions is shown in **Figure 9** (a). Arrows in **Figure 9** (a) indicate tests that met the runout condition. At all strain amplitudes, the SR+HIP+T6 treated specimens exhibited longer fatigue life than the SR+T6+HIP treated ones. At the tested strain amplitudes (0.003 and 0.002 mm/mm), the fatigue lives were well within the mid-cycle fatigue regime, where both fatigue crack initiation and crack growth lives were significant. Fractography of selected fatigue fracture surfaces at 0.003 mm/mm strain amplitude for SR+HIP+T6 and SR+T6+HIP conditions are presented in **Figure 9** (b) and (c), respectively. Both the SR+HIP+T6 and SR+T6+HIP treated specimens showed multiple crack initiation sites from the surface (**Figure 9** (b)-(c)).

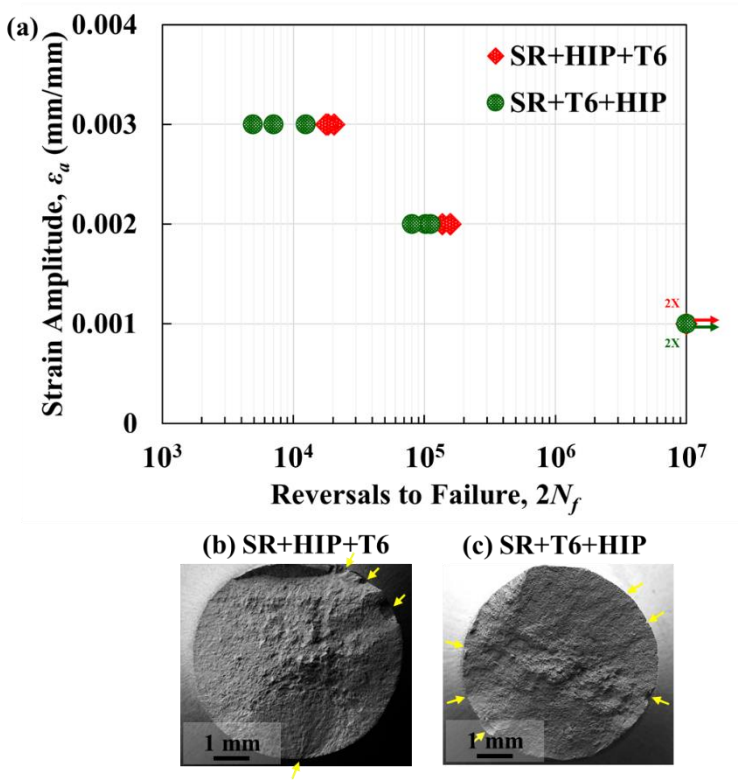

Figure 9. (a) Strain-life fatigue plot of L-PBF ALF357 specimens in two different HT conditions. Fracture surfaces of fatigue specimens in (b) SR+HIP+T6 and (c) SR+T6+HIP conditions tested at 0.003 mm/mm strain amplitude. The crack initiation sites are indicated by the yellow arrows.

Conclusions

This study investigated the effect of heat treatments (HT), consisting of two different sequences of stress relieving (SR), hot isostatic pressing (HIP), and T6 (i.e., SR+HIP+T6 and SR+T6+HIP) on the micro-/defect-structure and room temperature tensile and fatigue behaviors of AlF357 fabricated using laser powder bed fusion. The following conclusions were drawn:

- The SR+HIP+T6 treated specimens exhibited higher tensile strength but lower ductility compared to the SR+T6+HIP treated ones, which was attributed to the increased size and population of Mg_2Si and π-Fe particles in the SR+HIP+T6 condition.
- Specimens in the SR+HIP+T6 condition showed higher fatigue resistance for the alloy than those in the SR+T6+HIP condition.

Acknowledgments

This research is based upon the work partially funded by the National Aeronautics and Space Administration (NASA) under contract 80MSFC19C0010 and the National Science Foundation (NSF) under grant No. 2319690. This paper describes objective technical results and analysis. Any subjective views or opinions that might be expressed in the paper do not necessarily represent the views of the NASA or the United States Government.

References

[1] Esposito L, Bertocco A, Cricrì G, Rosiello V. Welding-repair effect on F357-T6 aluminum castings: analysis of fatigue life. Int J Adv Manuf Technol 2019;102:3699–706. https://doi.org/10.1007/s00170-019-03436-4.

[2] Michi RA, Plotkowski A, Shyam A, Dehoff RR, Babu SS. Towards high-temperature applications of aluminium alloys enabled by additive manufacturing. Int Mater Rev 2022;67:298–345. https://doi.org/10.1080/09506608.2021.1951580.

[3] Nickels L. AM behind the scenes. Met Powder Rep 2017;72:168–71. https://doi.org/10.1016/j.mprp.2017.04.027.

[4] Lathabai S. Additive Manufacturing of Aluminium-Based Alloys and Composites. In: Lumley RN, editor. Fundam. Alum. Metall., Elsevier; 2018, p. 47–92. https://doi.org/10.1016/B978-0-08-102063-0.00002-3.

[5] Tofail SAM, Koumoulos EP, Bandyopadhyay A, Bose S, O'Donoghue L, Charitidis C. Additive manufacturing: scientific and technological challenges, market uptake and opportunities. Mater Today 2018;21:22–37. https://doi.org/10.1016/j.mattod.2017.07.001.

[6] Ming X, Song D, Yu A, Tan H, Zhang Q, Zhang Z, et al. Effect of heat treatment on microstructure, mechanical and thermal properties of selective laser melted AlSi7Mg alloy. J Alloys Compd 2023;945:169278. https://doi.org/10.1016/j.jallcom.2023.169278.

[7] Theron M, Knutsen RD, Ivanchev LH, Burger HP. Effect of heat treatment on the properties of laser-beam welded rheo-cast F357 aluminum. J Mater Process Technol 2012;212:465–70. https://doi.org/10.1016/j.jmatprotec.2011.10.010.

[8] Hirsch SJ, Winter L, Grund T, Lampke T. Heat Treatment Influencing Porosity and Tensile Properties of Field Assisted Sintered AlSi7Mg0.6. Materials (Basel) 2022;15:2503. https://doi.org/10.3390/ma15072503.

[9] Pierre VC, Gokula KM, Pierrick B, Lore T, Brecht VH, Kim V. Reducing hydrogen pores and blisters by novel strategies and tailored heat treatments for laser powder bed fusion of AlSi7Mg0.6. Euro PM 2019 Congr Exhib 2019:1–7.

[10] Khan MF, Baig S, Ghiaasiaan SR, Gradl PR, Shao S, Shamsaei N. Effect of thermal post-processing on microstructure and tensile behavior of additively manufactured aluminum alloys (AlSi10Mg and Scalmalloy) via L-PBF: A comparative study. Solid Free Fabr 2022 Proc 33rd Annu Int Solid Free Fabr Symp – An Addit Manuf Conf 2022:341–53.

https://doi.org/10.26153/TSW/44158.

[11] Takata N, Kodaira H, Sekizawa K, Suzuki A, Kobashi M. Change in microstructure of selectively laser melted AlSi10Mg alloy with heat treatments. Mater Sci Eng A 2017;704:218–28. https://doi.org/10.1016/j.msea.2017.08.029.

[12] Prashanth KG, Scudino S, Klauss HJ, Surreddi KB, Löber L, Wang Z, et al. Microstructure and mechanical properties of Al–12Si produced by selective laser melting: Effect of heat treatment. Mater Sci Eng A 2014;590:153–60. https://doi.org/10.1016/j.msea.2013.10.023.

[13] Ma P, Prashanth K, Scudino S, Jia Y, Wang H, Zou C, et al. Influence of Annealing on Mechanical Properties of Al-20Si Processed by Selective Laser Melting. Metals (Basel) 2014;4:28–36. https://doi.org/10.3390/met4010028.

[14] ASTM International. ASTM E3: Standard Guide for Preparation of Metallographic Specimens. West Conshohocken, PA 19428-2959 USA 2012;03.01:1–12. https://doi.org/10.1520/E0003-11R17.

[15] ASTM International. ASTM E8/E8M Standard test methods for tension testing of metallic materials. West Conshohocken, PA 19428-2959 USA 2013. https://doi.org/10.1520/E0008.

[16] ASTM International. ASTM E606/E606M Standard Test Method for Strain-Controlled Fatigue Testing. West Conshohocken, PA 19428-2959 USA 2012. https://doi.org/10.1520/E0606-04E01.Copyright.

[17] Vanzetti M, Virgillito E, Aversa A, Manfredi D, Bondioli F, Lombardi M, et al. Short Heat Treatments for the F357 Aluminum Alloy Processed by Laser Powder Bed Fusion. Materials (Basel) 2021;14:6157. https://doi.org/10.3390/ma14206157.

[18] Khan MF, Nezhadfar PD, Gradl PR, Godfrey D, Diemann J, Shao S, et al. Investigate the height dependency of the micro-/defect-structure and mechanical properties of additively manufactured AlF357 aluminum alloy. Int. Solid Free. Fabr. Symp., 2022, p. 302–13. https://doi.org/10.26153/tsw/44148.